Effect of L-alanyl-glycine dipeptide on calcium oxalate crystallization in artificial urine

Polat, Sevgi; Eral, Huseyin Burak

DOI
10.1016/j.jcrysgro.2021.126176

Publication date
2021

Document Version
Final published version

Published in
Journal of Crystal Growth

Journal of Crystal Growth 566-567 (2021) 126176

Contents lists available at ScienceDirect

Journal of Crystal Growth

journal homepage: www.elsevier.com/locate/jcrysgro

Effect of L-alanyl-glycine dipeptide on calcium oxalate crystallization in artificial urine

Sevgi Polat [a,*], Huseyin Burak Eral [b,c]

[a] Department of Chemical Engineering, Faculty of Engineering, Marmara University, 34722 İstanbul, Turkey
[b] Van't Hoff Laboratory for Physical and Colloid Chemistry, Debye Institute for Nanomaterials Science Utrecht University, 3584 CH Utrecht, the Netherlands
[c] Process & Energy Laboratory, Delft University of Technology, 2628 CB Delft, the Netherlands

ARTICLE INFO

Communicated by S. Veesler

Keywords:
B1. Calcium oxalate monohydrate
B1. Calcium oxalate dihydrate
A1. Crystal Morphology
B1. Crystallization
A1. Phase transformation

ABSTRACT

Pathological crystallization of calcium oxalate (CaOx), the most common constituent of kidney stones, has attracted much attention due to recent surge in reported natural and synthetic additives effectively inhibiting its nucleation and growth. The aim of this study is to investigate the effect of L-alanyl–glycine (Ala–Gly), a dipeptide commonly found in human urine, on CaOx crystallization and its phase transformation in the presence of an artificial urine media. The nucleated CaOx crystals are characterized by XRD, FTIR, SEM, and dynamic light scattering in terms of changes in their crystalline form, morphology, and size. XRD and FTIR results revealed that Ala–Gly inhibited the formation of the thermodynamically most stable phase of CaOx, calcium oxalate monohydrate (COM) crystals. SEM images revealed that hexagonal plate-shaped COM crystals are transformed into the smaller tetragonal bipyramidal calcium oxalate dihydrate (COD) crystals with increasing additive concentrations. At 125 ppm Ala–Gly concentration more pronounced aggregation of CaOx crystals is observed accompanied with higher negative zeta potential value of -27.1 ± 2.9 mV. Moreover, the phase transformation from COM to COD is also confirmed through thermogravimetric analysis. Consequently, these results suggest that Ala–Gly has a profound effect on preventing the formation of COM crystals and helping to stabilize the COD crystals, a CaOx phase that is reported to have a lower tendency to stick to kidney cells thus decreasing the risk of stone formation. The reported suppression of COM in the presence of Ala–Gly might be significant to clinicians in their attempt to develop a long-term effective treatment for kidney stones.

1. Introduction

Deposits of minerals and organic compounds in the human urinary tract (kidney, ureter, and bladder), also known as kidney stones or urinary/renal calculi, occurs in ~12% of the world population and affects people under all socioeconomic conditions [1–3]. According to literature, conditions, such as high salt concentrations in the urine, pH, infections, and a decrease in the body's natural crystal inhibitors, may result in the formation of these stones. Kidney stone formation is a complex process of four sequential processes—nucleation, growth and aggregation, attachment, and retention [4–6].

Approximately 90% of kidney stones commonly comprise calcium oxalate (CaOx), calcium phosphate, and uric acid. Because CaOx is the most common constituent at 70–80%, CaOx crystallization and inhibition mechanisms have received the most attention in the literature [7–10]. CaOx crystallizes into the following three different forms: (1) calcium oxalate monohydrate (COM, $CaC_2O_4{\cdot}H_2O$, whewellite), a monoclinic crystal, (2) calcium oxalate dihydrate (COD, $CaC_2O_4{\cdot}2H_2O$, weddellite), a tetragonal crystal, and (3) calcium oxalate trihydrate (COT, $CaC_2O_4{\cdot}3H_2O$, caoxite), a triclinic crystal [11–14]. Kidney stones can comprise all three forms. Among these, COM is the most thermodynamically stable and the primary crystal within pathogenic stones. Because of its stability, COM is more difficult to remove in the urine than the more unstable COD and COT and it sticks more to the walls of the kidneys [15–17].

Surgical, drug, and ultrasonic treatments are the main methods by which kidney stones are treated; however, the results of these treatments are short termed and recurrence of stones at higher frequency after treatment has been reported. Several drugs have had positive effects on eliminating kidney stones; however, their therapeutic mechanisms remain unclear [18–20]. In addition to these drugs, natural and synthetic modifiers have been proposed in the literature. These additives

* Corresponding author.
E-mail address: sevgi.polat@marmara.edu.tr (S. Polat).

https://doi.org/10.1016/j.jcrysgro.2021.126176
Received 28 February 2021; Received in revised form 3 May 2021; Accepted 5 May 2021
Available online 11 May 2021

interfere with the nucleation and/or growth of CaOx or induce COT or COD formation instead of COM. Crystal growth modifiers are small amounts of additives that can be used to either promote or inhibit crystallization/transformation processes. Several types of additives, such as amino acids [21–28], proteins [29,30], carboxylic acids [31–33] and polymers [34–36] have been shown to affect CaOx crystallization. In addition, studies have shown that peptides containing aspartic acid-glutamic acid, glutamic acid-glutamic acid, alanine-aspartic acid amino acids have a profound effect on the CaOx crystals and could promote the formation of COD and COT crystals and stabilize these metastable phases over very long periods of time [37–42]. Therefore, the investigation of peptide effects on the CaOx crystallization process, especially inhibition of COM crystals, is highly significant. Some reports have shown the roles that alanine and glycine as individual additives have on CaOx crystallization [22,27]. However, the combined effect of these additives has not been reported. The present study aimed to elucidate the combined effects of adding $CH_3CH(NH_2)CONHCH_2COOH$ (L-alanyl–glycine or Ala–Gly), a dipeptide, on CaOx crystallization in an artificial urine medium. The structural, morphological, and thermal characterization of the obtained crystals are detailed in this report.

2. Materials and methods

2.1. Materials

Calcium chloride dihydrate ($CaCl_2{\cdot}2H_2O$) and sodium oxalate ($Na_2C_2O_4$) used as reactants were analytically pure and obtained from Merck (Darmstadt, Germany). Ala–Gly used as the additive was purchased from Sigma-Aldrich (Gillingham, UK) and used without further purification. Distilled water was used in all experiments.

2.2. Experimental methods

The CaOx crystals were synthesized as a result of the reaction between $CaCl_2$ and $Na_2C_2O_4$ solutions in a double-jacketed crystallizer with an active volume of 500 mL. The experiments were conducted at 37 °C and 400 rpm. The temperature was controlled by a thermostat with an accuracy of ±0.1 °C, and a mechanical stirrer equipped with a three-bladed propeller installed in the center of crystallizer was used. To monitor the pH and keep it constant, a pH meter was connected to an automated pH control unit and the pH of the solution was adjusted to 6.5 using 0.05 M HCl (aq) and NaOH (aq). The experimental setup is shown in Fig. 1.

At the beginning of the experiment, 0.5 M stock solutions of $CaCl_2$ and $Na_2C_2O_4$ were prepared by dissolving an appropriate quantity of each reagent in artificial urine. The artificial urine was prepared as described in Miyake et al. [43] and Dong and Wu [44] and its composition was as follows: 0.01695 M Na_2SO_4, 0.00385 M $MgSO_4{\cdot}7H_2O$, 0.0455 M NH_4Cl, 0.0637 M KCl, 0.1055 M NaCl, 0.0323 M NaH_2PO_4, and 0.00321 M $Na_3C_6H_5O_7$. The solution was filtered through a 0.22-μm membrane filter before use.

To synthesize the CaOx crystals, 0.5 M $CaCl_2$ solution was placed into the crystallizer and left to reach thermal equilibrium for 30 min, after which 0.5 M $Na_2C_2O_4$ solution was continuously fed into the crystallizer at a rate of 4 mL/min using a peristaltic pump. The total volume of each experimental solution was 200 mL. After continuously stirring for 1 h, the final suspension was filtrated using a 0.45-μm Millipore membrane filter, rinsed thoroughly three times with distilled water and ethanol, and dried at room temperature. The dried samples were used in the analyses. All experimentation was performed in triplicate.

To investigate the effects Ala–Gly and its concentration on the crystallization processes, specific amounts of the modifier were added to the $CaCl_2$ solution before adding the $Na_2C_2O_4$ solution. The concentration of Ala–Gly ranged from 0 to 125 ppm.

2.3. Characterization

LabX X-ray diffraction (XRD-6100; Shimadzu) using a CuKα radiation source was used to analyze the structure and crystalline forms of the obtained crystalline particles. Analyses were performed at 40 mV and 30 mA over a 2θ range of from 10 to 70° at a rate of 2°/min. Quantitative phase analysis of the samples was accomplished using the Rietveld refinement method [45] employing the Materials Analysis Using Diffraction (MAUD) software (developed by Wenk, Matthies & Lutterotti and Ferrari & Lutterotti). The functional groups of the crystals were identified using the IR Affinity-1 Fourier transform infrared

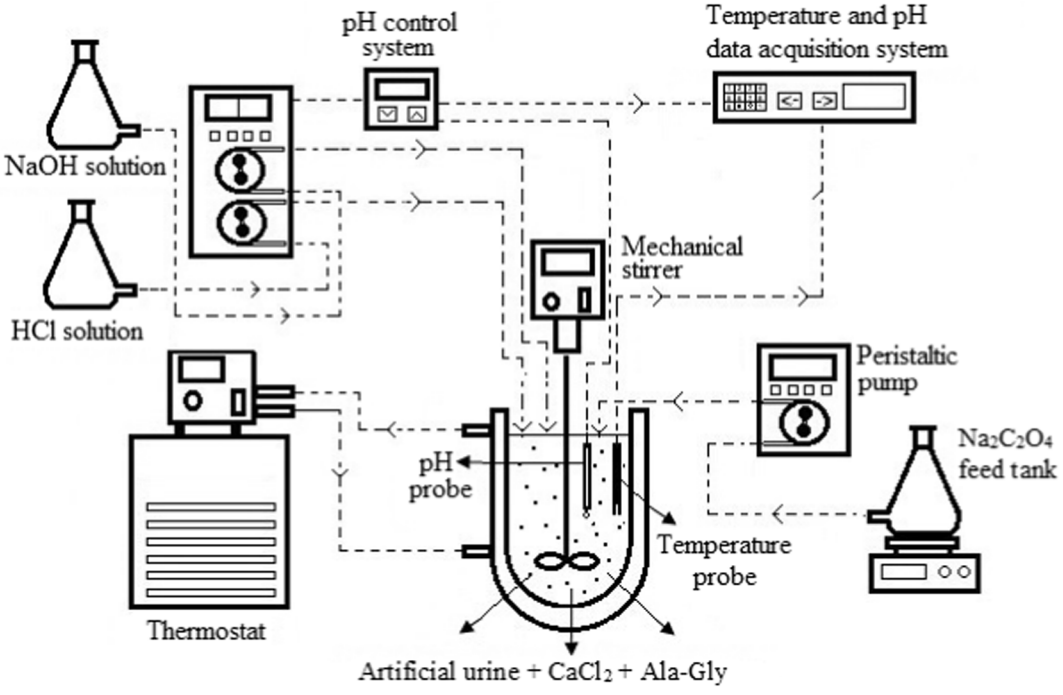

Fig. 1. Experimental setup.

spectroscope (FTIR; Shimadzu) equipped with ATR accessories. Measurements were conducted at room temperature between 600 and 4000 cm^{-1} in transmission mode with a resolution of 4 cm^{-1}. The surface morphology of the obtained crystalline particles was observed using the EVO LS 10 scanning electron microscope (SEM; Zeiss). The particle size of the samples was calculated by the image analysis software based on a predefined scale. The calculation was conducted using over 100 number of crystals and different SEM images of a sample to improve the accuracy of the results. The volume-based particle size distribution was measured using the Mastersizer 2000 laser particle size analyzer (Malvern Panalytical, Malvern, UK). The zeta potential (ζ potential) of the samples was measured using the Zeta Sizer Nano Series Nano-ZS (Malvern). Each measurement was repeated at least 10 times, and the average value was calculated. All experiments were performed at 25 °C and pH 6.5. The thermal behavior of the samples was determined using the SDT Q600 thermogravimetric analyzer (TA Instruments) from 25 to 1000 °C at a heating rate of 20 °C/min. High purity nitrogen (99.999%) with a flow rate of 30 mL/min was used as carrier gas to maintain the inert atmosphere. The simultaneous evolution of the gases during thermal decomposition was detected using the Tensor27 FTIR (Bruker) coupled with thermogravimetric analysis (TGA) with a heating rate of 20 °C/min. The transfer line from TGA to FTIR was kept at 200 °C to avoid gas condensation.

3. Results and discussion

3.1. XRD and FTIR

Resulting crystals were analyzed to determine the crystalline structure and hydrates of the CaOx crystals obtained with and without the additive. The XRD patterns for the samples obtained with different concentration of Ala–Gly within the range of 10–70° are presented in Fig. 2a.

As shown in Fig. 2a, the XRD pattern for the crystals obtained in the artificial urine media without any additive showed COM (Joint Committee on Powder Diffraction Standards [JCPDS]: 00–020-0231) as the only crystalline product. Neither any of the other hydrate phases nor impurities were detected, which indicated that the product was highly pure within the accuracy of XRD. All main diffraction peaks observed at 14.94, 24.52, 30.22, 36.14, and 38.18° corresponded to the (101), (020), (202), (112), and (130) lattice planes of the monoclinic COM crystal structure, respectively. The refined unit cell parameters of the crystals obtained in pure media were calculated to be $a = 6.2917$ Å, $b = 14.5823$ Å, $c = 10.1171$ Å, $\beta = 109.43°$, and cell volume (V) = 875.35 Å (Table 1). These results agreed with those reported from earlier studies [46,47]. Similar to that in pure media, the crystals obtained in the presence of 25 ppm Ala–Gly were pure COM. There was no change in crystal structure, which indicated that the presence of 25 ppm additive had no effect on the crystal form. At Ala–Gly concentration of 50 ppm, a new crystalline phase was detected in addition to the COM phase. The new peaks appeared at 14.34° (200), 20.08° (211), 28.88° (400), 32.22° (411), and 40.20° (213) and coincided with JCPDS: 00–017-0541, which were characteristic of the COD crystalline structure. That is, the characteristic diffraction peaks of both COM and COD appeared together, which indicated partial phase transformation from COM to COD. The COM diffraction peaks weakened as the corresponding main COD diffraction peaks grew stronger. Using Rietveld refinement quantitative analysis, the mass fractions of COM and COD forms for the samples obtained at 50 ppm Ala–Gly were 35.4 and 64.6%, respectively. As Ala–Gly concentration increased, the diffraction peak intensity of COD increased, while the corresponding diffraction peak intensity of COM decreased. Such results suggest that as the concentration of the additive increased, the COD amount increased. When the Ala–Gly concentration was at 75 ppm, nearly all of the COM peaks completely disappeared and all peaks detected were related to the COD form. According to Rietveld refinement results, the mass fractions of COM and

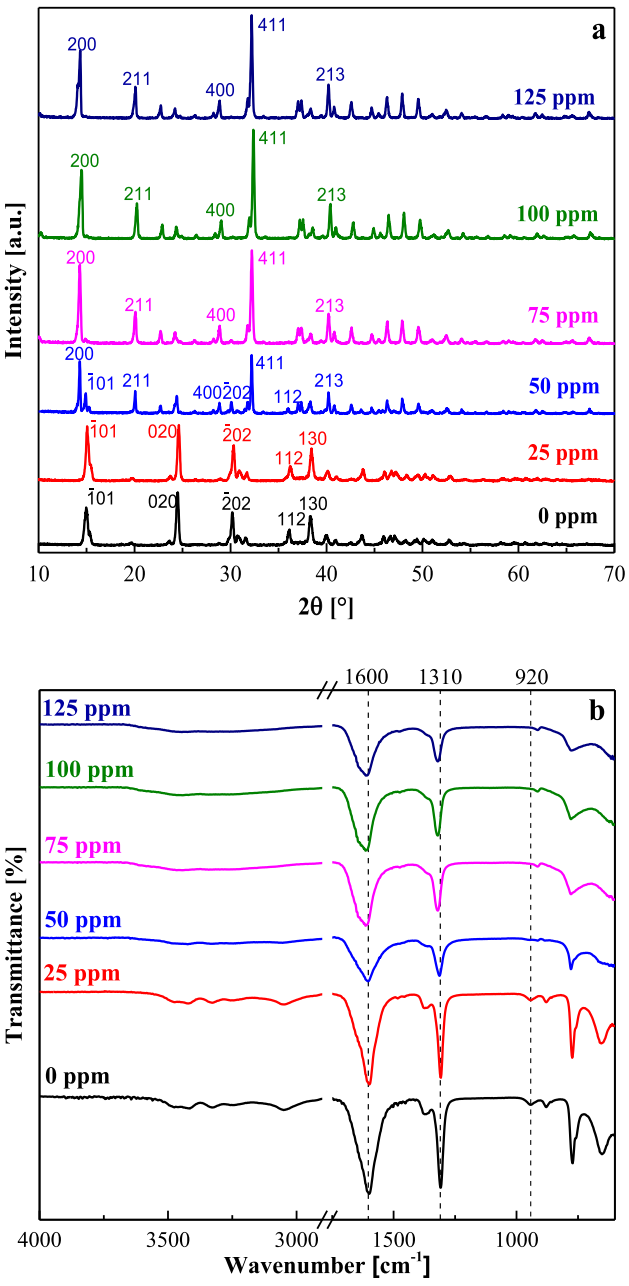

Fig. 2. a) XRD results and b) Fourier-transform infrared spectroscopy results for the calcium oxalate (CaOx) crystals obtained at different concentrations of L-alanyl–glycine (Ala–Gly). Black: 0 ppm, red: 25 ppm, blue: 50 ppm, magenta: 75 ppm, olive: 100 ppm, navy: 125 ppm.

COD were determined to be 2.5 and 97.5%, respectively. At 100 and 125 ppm Ala–Gly, the characteristic peaks corresponding to the COM form transformed completely into those corresponding to the COD form. Thus, the Ala–Gly dipeptide at different concentrations had a significant effect on the CaOx hydrates and led to the formation of the COM to COD phase.

FTIR analyses were conducted to further ascertain the transformation process from COM to COD and identify the functional groups of the crystals. The COD form showed an FTIR spectrum that was significantly different from that of the COM form, which enabled detection of phase transformation. The FTIR spectra for the crystals obtained in the absence and presence of different concentrations of Ala–Gly dipeptide are illustrated in Fig. 2b. We observed from Fig. 2b that all the main characteristic absorption bands of COM were seen in

Table 1
Unit-cell parameters and distribution of the calcium oxalate (CaOx) phase in the products obtained using different L-alanyl-glycine (Ala–Gly) concentrations.

L-alanyl-glycine (Ala-Gly) (ppm)	Phase	Wt (%)	Unit cell dimensions				
			a (Å)	*b* (Å)	*c* (Å)	*β* (°)	*V* (Å)
0	COM	100	6.2917	14.5823	10.1171	109.43	875.35
25	COM	100	6.2983	14.6028	10.1166	109.39	877.68
50	COM	35.4	6.2942	14.5863	10.1162	109.43	875.86
	COD	64.6	12.369		7.3548		1125.23
75	COM	2.5	6.3164	14.5411	10.1166	109.38	876.53
	COD	97.5	12.375		7.3585		1126.89
100	COD	100	12.378		7.3610		1127.81
125	COD	100	12.384		7.3616		1129.00

the FTIR spectra for the crystals obtained in the absence of the additive. Consistent with the XRD results, the COM crystals prepared without Ala–Gly dipeptide were pure products. The five absorption peaks between 3510 and 2950 cm^{-1} are attributed to the O—H bond of crystal water in the samples. Moreover, the absorption peaks of COM were detected at ~950 cm^{-1} (C—O stretching vibration), 880 cm^{-1} (C—C stretching vibration), and 661 cm^{-1} (O—C—O plane bending vibration) [44,47–49]. The crystals obtained with 25 ppm additive consisted of COM forms similar to those in pure media. No difference was observed after adding 25 ppm Ala–Gly to the crystallization medium, and no new crystallization product was found. The FTIR spectrum for 50 ppm additive showed that COM crystals partially converted to COD forms, a result cooperated with XRD given in Fig. 2. After adding 50 ppm Ala–Gly to the medium, the COM peaks gradually weakened while new COD peaks appeared. In addition, the FTIR characteristics of the COD form were different from those of the COM form. The most obvious change in the FTIR shift occurred at 1600 and 1305 cm^{-1} in the samples, and these peaks shifted toward 1604 and 1312 cm^{-1}. This shifting was related to COD/COM ratio in the mixture; therefore, we suggest that the crystals prepared using the 50 ppm Ala–Gly were forms of both COM and COD. The crystals obtained in 75 ppm additive medium were nearly completely converted to COD form, and the characteristic COM peaks subsequently weakened. At 100 and 125 ppm Ala–Gly concentration, FTIR spectra indicate that the characteristic absorption peaks of the

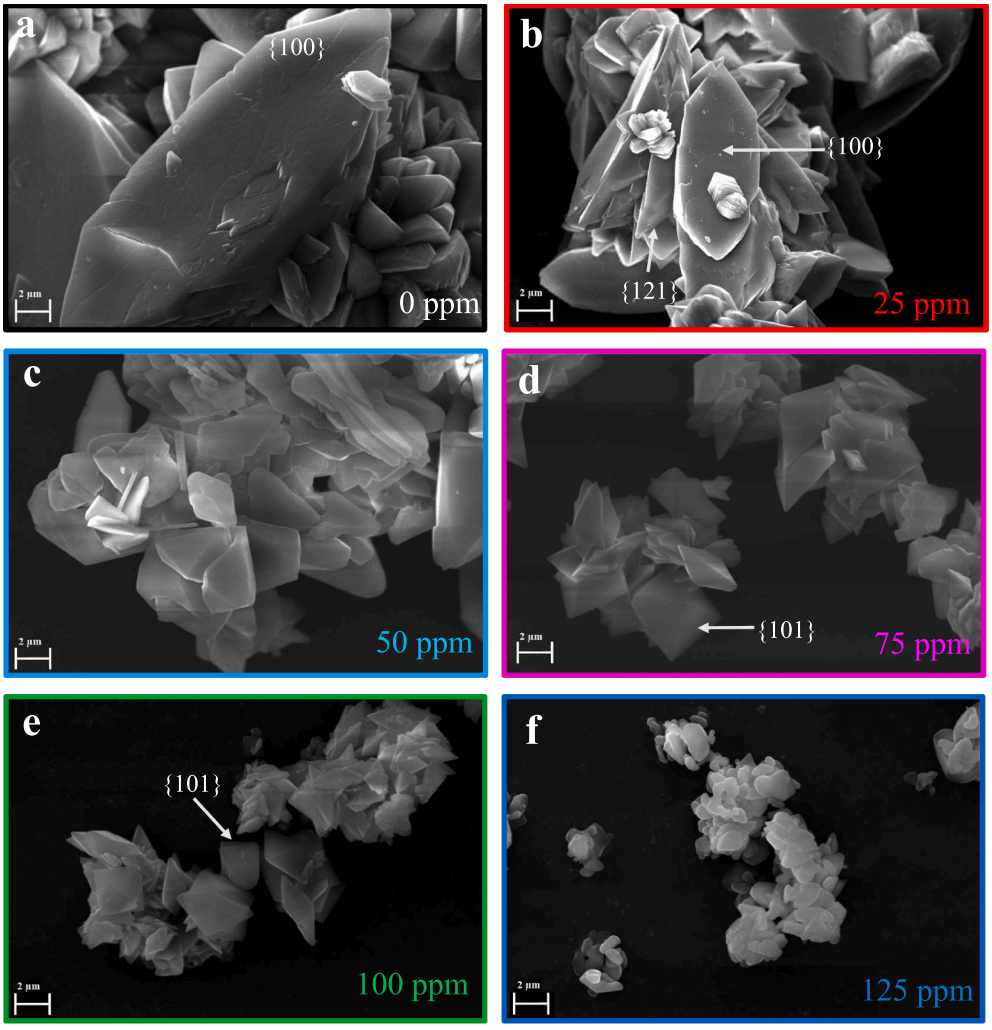

Fig. 3. Scanning electron microscopy images of the calcium oxalate (CaOx) crystals obtained at different concentrations of L-alanyl–glycine (Ala–Gly). a) 0 ppm, b) 25 ppm, c) 50 ppm, d) 75 ppm, e) 100 ppm, f) 125 ppm.

COM form no longer existed, which meant that the COM crystals had completely transformed into the COD form. That is, with higher concentrations of Ala–Gly, the resulting crystals consisted of only the COD form, which was consistent with the XRD results. In addition, when compared to the COM spectrum, one strong peak at ~3400 cm^{-1} was obtained only within the range of 3510–2950 cm^{-1} and there were no weak bands. A new peak located at ~915 cm^{-1} was related to the COD form.

3.2. SEM

The effect of different Ala–Gly concentrations on the morphology of CaOx crystals was investigated using SEM. In addition to XRD and FTIR analyses, CaOx hydrates were determined using SEM on the basis of morphological criteria because COM crystals with hexagonal shape are easily distinguished from COD forms with tetragonal bipyramidal appearance. The SEM images and particle-size distribution results are illustrated in Figs. 3 and 4, respectively.

The SEM image in Fig. 3a shows that CaOx crystals obtained without Ala–Gly were composed of the aggregated and most thermodynamically stable form of CaOx, the COM crystals. The COM crystals, the largest face of which was observed at {1 0 0}, had a hexagonal plate-shaped morphology and included penetrated twins consisting of these hexagonal particles. This morphology confirmed the findings from previous studies [50,51]. At the {1 0 0} surface of the hexagonal crystals, the new crystal formation could be observed, which led to the formation of intertwined crystals during their additional growth stages. The mean particle size of the crystals was 20.0 μm with standard deviation of 1.1 measured from SEM images. As shown in Fig. 3b, similar to that seen without the additive media, the CaOx crystals obtained in the presence of 25 ppm Ala–Gly had smaller individual and twinned hexagonal COM crystals with irregular surfaces and intertwined growth. As shown in Fig. 3b, similar to that seen without the additive media, the CaOx crystals obtained in the presence of 25 ppm Ala–Gly had smaller individual and twinned hexagonal COM crystals with irregular surfaces and intertwined growth. That is, the presence of 25 ppm additive had very little effect on COM morphology, but the size of the crystals decreased by ~50% compared to that in pure media. The mean particle size of crystals obtained was 9.9 μm with standard deviation of 0.8 measured from SEM images. Moreover, the new COM crystal formation was observed on the {1 0 0} and {1 2 1} faces of the COM with a tendency for aggregation. Upon increasing the Ala–Gly concentration to 50 ppm, a distinct change in CaOx morphology and size was observed. As shown in Fig. 3c, both COM and COD crystals were observed, which was consistent with the results of the XRD and FTIR analyses. A new structure emerged as a result of the intertwined formation of two different forms—hexagonal COM and tetragonal bipyramidal prisms of COD crystals. Compared to 25 ppm Ala–Gly, there was less formation of COM, with tetragonal bipyramids crystals being more abundant in the crystalline products. The crystals were smaller compared to those in the pure media and 25 ppm additive, and slightly aggregated crystals were obtained. As shown in Fig. 3d, the results of 75 ppm Ala–Gly were similar to that in 50 ppm but with smaller crystals. The mean particle size of the crystals was 4.2 μm with standard deviation of 0.7 measured from SEM images. The CaOx crystals were nearly completely in COD form, and new COD crystal formation in the {1 0 1} faces could be observed. In the presence of 100 ppm Ala–Gly, the crystalline products consisted mainly of uniform tetragonal bipyramidal COD crystals with a mean size of ~3.5 μm, as shown in Fig. 3e. These crystals had sharp edges and corners. At the Ala–Gly concentration of 125 ppm, all CaOx crystals were the COD forms and consisted of weak and thinner aggregates. In other words, crystal morphology was more variable with a decrease in particle size at that concentration. As is clearly shown in Fig. 3f, the formed COD crystals lost their tetragonal bipyramidal appearance, which was replaced by quadrilateral forms with rounded edges. The COD crystals obtained were also in the form of thin plates, and new COD crystals in plate form were created. This also revealed that the tendency for aggregation clearly decreased with an increase in Ala–Gly concentration. The 125 ppm Ala–Gly had the most enhanced effect on crystal morphology, size, and aggregation. To sum up, SEM images in Fig. 3

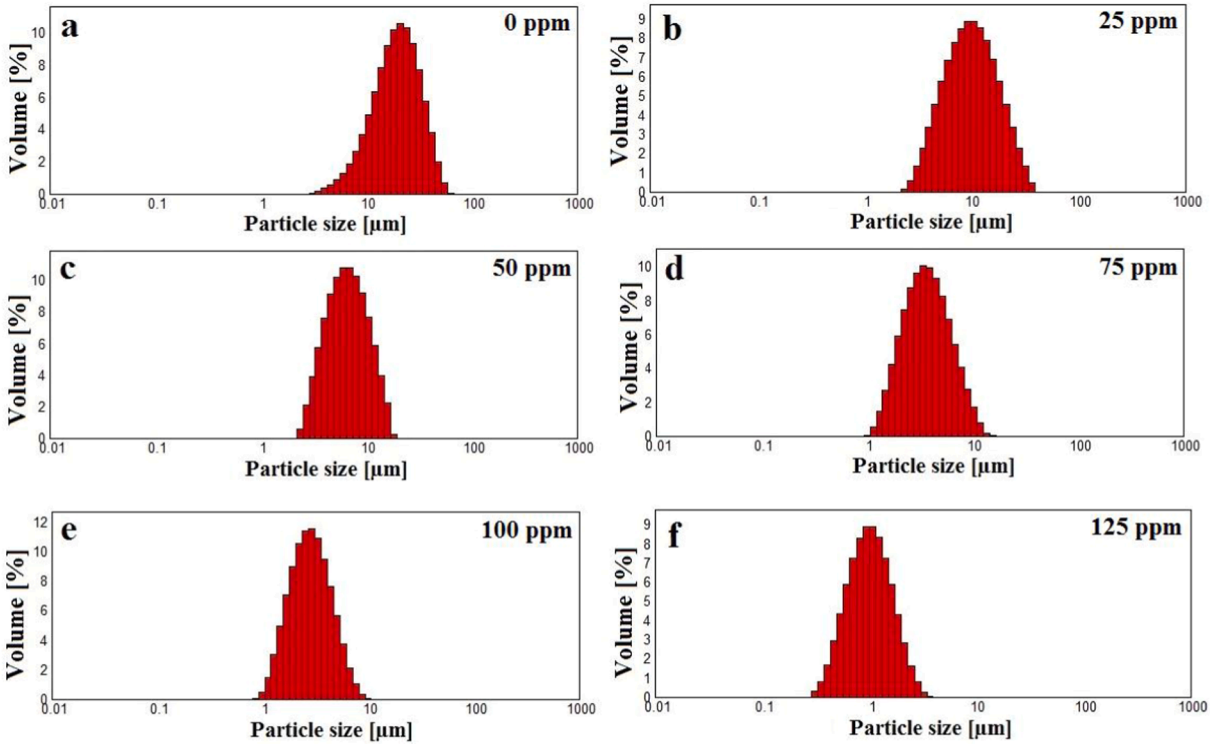

Fig. 4. Particle size distributions of the calcium oxalate (CaOx) crystals obtained at different concentrations of L-alanyl–glycine (Ala–Gly). a) 0 ppm, b) 25 ppm, c) 50 ppm, d) 75 ppm, e) 100 ppm, f) 125 ppm.

confirmed the deduced phase transformation from COM to COD from the XRD and FTIR analyses.

When the results of the SEM and particle size analyses were examined together, we conclude that presence of Ala–Gly alters not only the hydrate form crystalizing from artificial urine but also the crystal morphology and the average crystal size. Several hypotheses have been put forward to explain the mechanism through which modifiers affect COM crystallization. One suggestion is that impurities are adsorbed on the face of the crystals or enter the crystals, while another report proposed that the degree of hydration of COM leads to the formation of a metastable phase of COD [7,8]. The results of the current study suggest that Ala-Gly inhibits the growth of COM crystals and has a significant impact on their size. While conversely the degree of aggregation of the crystals decreases with the addition of Ala-Gly and some COD is formed.

As stated in the literature [52,53], the ability of COM and COD crystals to adhere to the walls of the kidneys and/or renal tubules differ. The reduced adhesion characteristic of COD compared to COM allows it to be expelled more easily than COM crystals from the kidneys or tubules with the urine. The COM crystals tend to be retained within the urinary system, which then induces stone formation. Therefore, we rationalize that CaOx crystals in COD form with smaller average crystal size will be taken out of the kidney easier with less chance of retention. Consequentially we speculate that the presence of Ala–Gly in urine can have therapeutic effect reducing urinary stone formation.

3.3. Zeta potential

The ζ potential of the CaOx crystals obtained using different concentrations of Ala–Gly was measured to determine the surface charge and stability of the samples. The results are depicted in Fig. 5.

The CaOx crystals obtained in artificial urine media without Ala–Gly had a negative surface charge (−5.8 ± 0.6 mV). At 25 and 50 ppm Ala–Gly, a slight increase in negativity was clearly observed in the ζ potential value of the CaOx crystals. This change in the ζ potential may suggest that the Ala–Gly could be adsorbed onto the CaOx crystals, leading to an increase in the absolute value of the ζ potential of the crystals and an increase in the electrostatic repulsion force between the crystals. As the Ala–Gly concentration increased, the ζ potential value of CaOx distinctly rose, which clearly illustrated that the electrical surface charge of CaOx was more negative at a higher Ala–Gly concentration due to the crystal surface being covered with the negatively charged ions of the additive. The ζ potential values at 75 and 100 ppm Ala–Gly were −15.5 ± 1.2 mV, and −23.6 ± 1.7 mV, respectively. ζ Potential is a key indicator of the stability of a suspension of particles. Generally, these particles at ζ −30 mV > ζ > 30 mV can be considered stable [54], which indicates that particles with ζ potentials >+30 mV or less than −30 mV are normally considered electrically stable, while the particles with a ζ potential within the range of ⟨−30 mV, +30 mV⟩ tend to aggregate. Taking this expression in account, we suggest that the suspension of CaOx crystals obtained at higher additive concentrations was the most stable and slightly tend to aggregate. When increasing Ala–Gly concentration to 125 ppm, this tendency was more distinct because the ζ potential decreased and the value reached −27.1 ± 2.9 mV, which suggested a strong interparticle repulsive force that then improved suspension stability and reduced aggregation. These results are consistent with those seen on the SEM images.

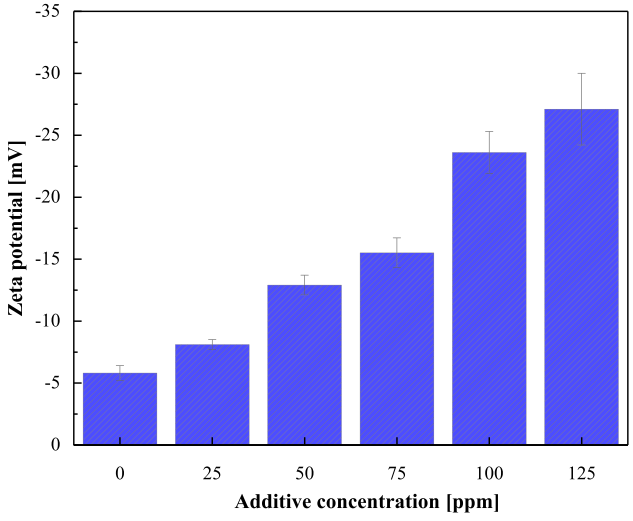

Fig. 5. The zeta potential of calcium oxalate (CaOx) as a function of L-alanyl–glycine (Ala–Gly) concentration.

3.4. TGA/FTIR

TGA has been extensively used to analyze kidney stones because of its ability to produce fast and quantitative results [55]. The decomposition patterns of the crystals obtained with and without Ala–Gly at 20 °C/min are shown in TGA and derivative thermogravimetric (DTG) curves (Fig. 6).

In accordance with the literature [56,57], the thermal decomposition of COM crystals consisted of three weight-loss stages as shown below with the overall reaction equations.

Overall reaction: $CaC_2O_4.H_2O \rightarrow CaO + H_2O + CO + CO_2$

$$CaC_2O_4.H_2O \rightarrow CaC_2O_4 + H_2O \quad (1)$$

$$CaC_2O_4 \rightarrow CaCO_3 + CO \quad (2)$$

$$CaCO_3 \rightarrow CaO + CO_2 \quad (3)$$

As shown in Fig. 6a, the first stage in which there was a weight loss of 12.3% between 88 and 201 °C included the loss of the water of crystallization to form anhydrous CaOx. At temperatures from 415 to 515 °C, a second weight loss of 19.0% was observed, which corresponded to the decomposition of anhydrous CaOx with the loss of CO. The last stage resulted in the most weight loss (30.2%) between 646 and 767 °C and involved the decomposition of calcium carbonate into calcium oxide with the loss of CO_2. After the third stage, the weight stabilized at 38.5%. The obtained weight-loss values matched the theoretical values of the COM crystals. Thus, the TGA and DTG curves further proved that the crystals obtained in pure media were COM forms. As shown in Fig. 6b, the curves showed a similar decomposition behavior and weight loss in pure media. The total weight loss was 61.6% of the initial weight. That is, consistent with the results of XRD and FTIR, the crystals obtained in 25 ppm Ala–Gly were those of COM. At higher concentrations of Ala–Gly (Fig. 6c), the new DTG peak observed within the temperature range of ~40–100 °C was attributed to the removal of the adsorbed water from the COD crystals. Although this peak intensity was very weak in 50 ppm Ala–Gly and showed the partial transformation of COM into COD crystals, the corresponding peak was stronger at higher concentrations, which indicated the full conversion from COM to COD.

After increasing the Ala–Gly concentration (Fig. 6d–f), the total weight loss increased. Based on the TGA/DTG curves for the crystals obtained with 100 and 125 ppm Ala–Gly, the solid residue was ~34%, which agreed with the theoretical values at the end of the decomposition process that showed that the crystals obtained were mainly the COD form. Moreover, Fig. 6 indicated that the crystals did not include any Ala–Gly additive in the samples but that it also controlled the crystallization process.

Although TGA provided beneficial information about the thermal decomposition characteristics of the samples, the combined thermal and spectroscopic techniques, such as TGA/FTIR, are practical ways by which to explain the evolved gasses during the decomposition process; therefore, the analysis of evolved gases using FTIR was simultaneously conducted to help identify the gases. Using this combined approach, the

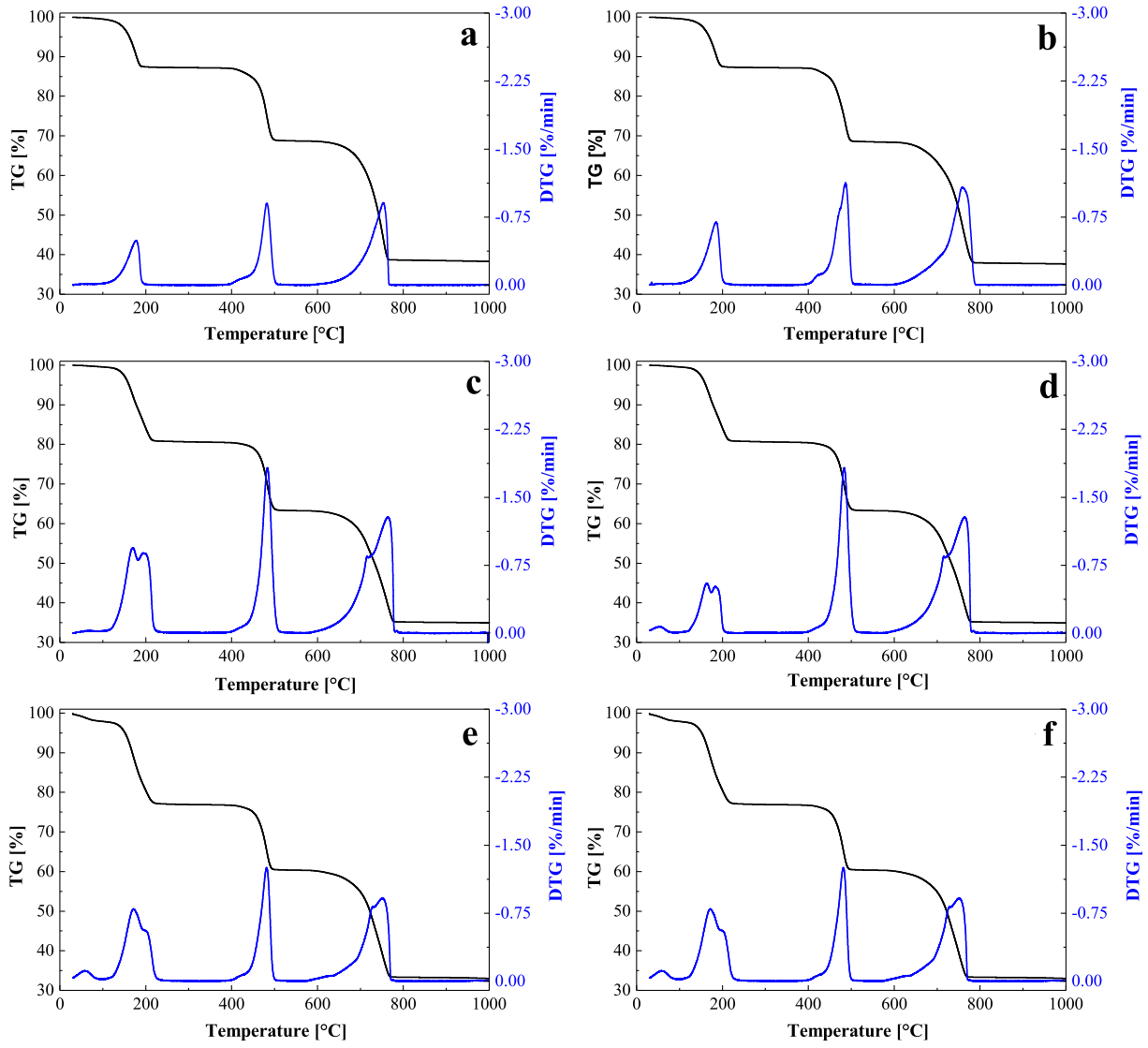

Fig. 6. Thermogravimetric analysis (TGA) and derivative thermogravimetric (DTG) curves for the calcium oxalate (CaOx) crystals obtained at different concentrations of L-alanyl–glycine (Ala–Gly). a) 0 ppm, b) 25 ppm, c) 50 ppm, d) 75 ppm, e) 100 ppm, f) 125 ppm.

exact sample that was decomposed was identified and recorded at each temperature. FTIR generates a Gram–Schmidt (GS) profile of total absorbance intensity based on time/temperature, and this profile indicates how the concentration of the evolved gases varies during the thermal decomposition process. Fig. 7 illustrates the GS profiles obtained for the CaOx crystals with and without Ala–Gly.

As shown in Fig. 7, the GS profiles of all samples correlated directly with the stages in the TGA curves. Although three different peaks were observed in the GS curves during the decomposition of the COM crystals, COD crystals had an extra weak peak between ~60 and 270 sec (corresponding to 45–115 °C), which was similar to that in the DTG curves. Compared to the DTG curves, only the peak temperature in the GS curves shifted slightly toward the higher region because of a small time delay in the transport of the evolved volatiles from TGA to FTIR.

The three-dimensional (3D) FTIR spectra indicated the change in spectral intensity over time, and the wavelength for the crystals obtained with and without Ala–Gly is provided in Fig. 8. In addition, the instantaneous FTIR spectra of the evolved species during thermal decomposition of the crystals at the maximum peak temperature for all three stages are shown in Fig. 9.

The FTIR spectra of the evolved gases at ~190 °C confirmed that the weight loss was a result of water vapor (band between 3000 and 3500 cm^{-1}) evolving from the samples. Compared with the 3D FTIR spectra for the crystals with and without Ala–Gly, we clearly observed that the absorption intensity of O–H stretching vibration increased with an increase in Ala–Gly concentration, which confirmed the transformation of COM into COD forms. The FTIR spectra at 490 °C confirmed that CO gas evolved with the two peaks close to 2100 cm^{-1}; however, peaks at 667 and 2350 cm^{-1} indicated that CO_2 was also produced during the second stage. CO_2 formed as a result of the disproportionate reaction of CO into CO_2. The peaks at 667 and 2350 cm^{-1} in the FTIR spectra at ~780 °C confirmed the evolution of CO_2 in the final stage. No evolved gases characterizing Ala–Gly additive were observed for the samples, possibly because the very small amount of additive that was adsorbed by the crystal surface was below the limit of detection for the instrument. As a result of using TGA/FTIR analyses on the samples, we detected that the main evolved products were water, CO, and CO_2. These results were consistent those in the studies of CaOx thermal decomposition [56–58].

To sum up; our experiments show that increasing Ala–Gly concentration gradually to 125 ppm promotes COD formation at 37 °C and fixed pH 6.5, decreases the effective crystal size and leads to increase in the measured absolute surface charge. The observed results can arise through two scenarios: (I) preferred nucleation and growth of COD over COM or (II) preferred nucleation but inhibited growth of COM followed

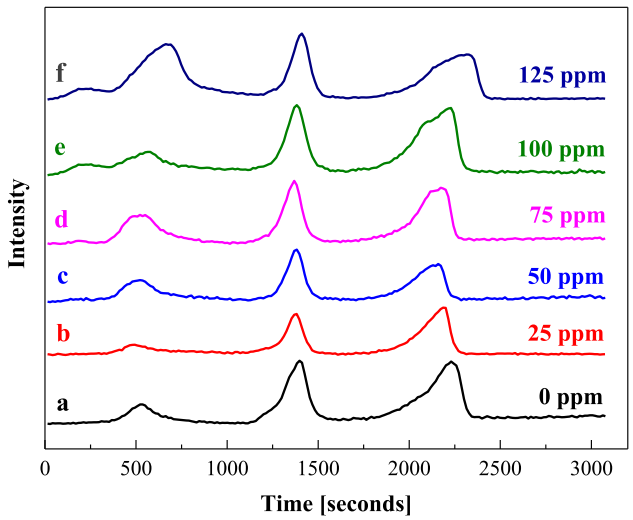

Fig. 7. Gram-Schmidt curves for the calcium oxalate (CaOx) crystals obtained at different concentrations of L-alanyl–glycine (Ala-Gly). a) 0 ppm, b) 25 ppm, c) 50 ppm, d) 75 ppm, e) 100 ppm, f) 125 ppm.

by preferred growth of COD at elevated Ala–Gly concentrations. For scenario I, we hypothesize that the higher density of H-bonding groups at high Ala–Gly concentration might lower the relative nucleation energy barrier of COD compared to COM hence promoting COM suppression at high Ala–Gly concentrations. Consequently, enhanced COD nucleation rate can consume available supersaturation rapidly, resulting in smaller COD crystals. We further hypothesize that, once the COD crystals nucleate, the enhanced absolute surface charge due to Ala–Gly adsorption renders COD suspensions more stable in solution. In the context of scenario I, we tentatively propose that Ala–Gly may influence the in-vitro CaOx crystallization under studied conditions with a two-step mechanism consisting of a hydrate form selection step promoted by H-bonding followed by suspension stabilization initiated by Ala–Gly adsorption. For scenario II to occur, adsorption of Ala–Gly has to preferentially to promote COD growth at a rate large enough to overcome the initially dominant COM nucleation. It should be noted that proving which scenario is dominating the current study is a colossal undertaking requiring equilibrium solubility measurements of COM and COM in the presence of Ala–Gly without promoting hydrate transition. Such measurements are extremely challenging due to low solubility of CaOx in artificial urine and beyond the scope of this study.

4. Conclusions

The present study shows that presence of dipeptide Ala–Gly influences CaOx crystallization in artificial urine. Based on the XRD and FTIR analyses, COM was found to be the only crystalline phase present in CaOx crystallized from artificial urine when equimolar aqueous $CaCl_2$ and $Na_2C_2O_4$ solutions react at 37 °C and constant pH 6.5. However, at

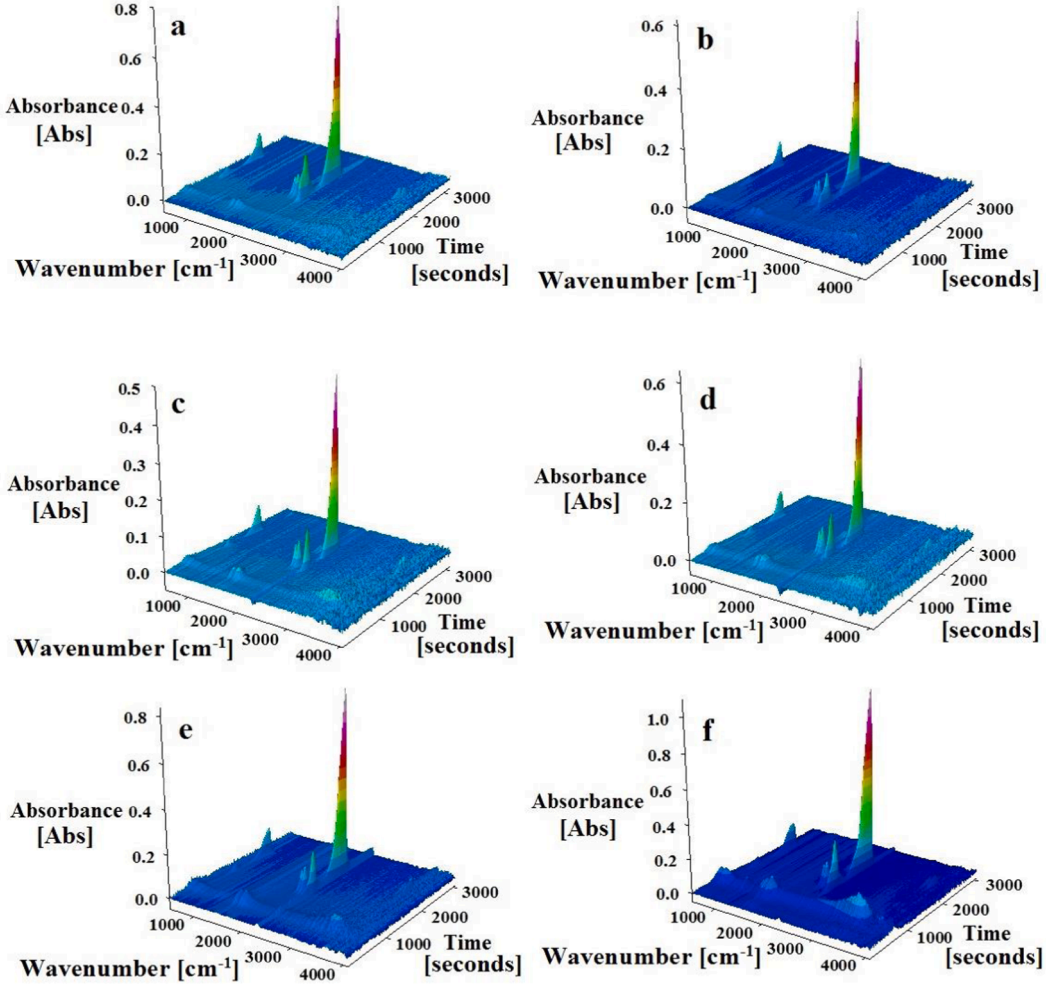

Fig. 8. Three-dimensional Fourier-transform infrared spectroscopy (FTIR) spectra for the calcium oxalate (CaOx) crystals obtained at different concentrations of L-alanyl–glycine (Ala–Gly). a) 0 ppm, b) 25 ppm, c) 50 ppm, d) 75 ppm, e) 100 ppm, f) 125 ppm.

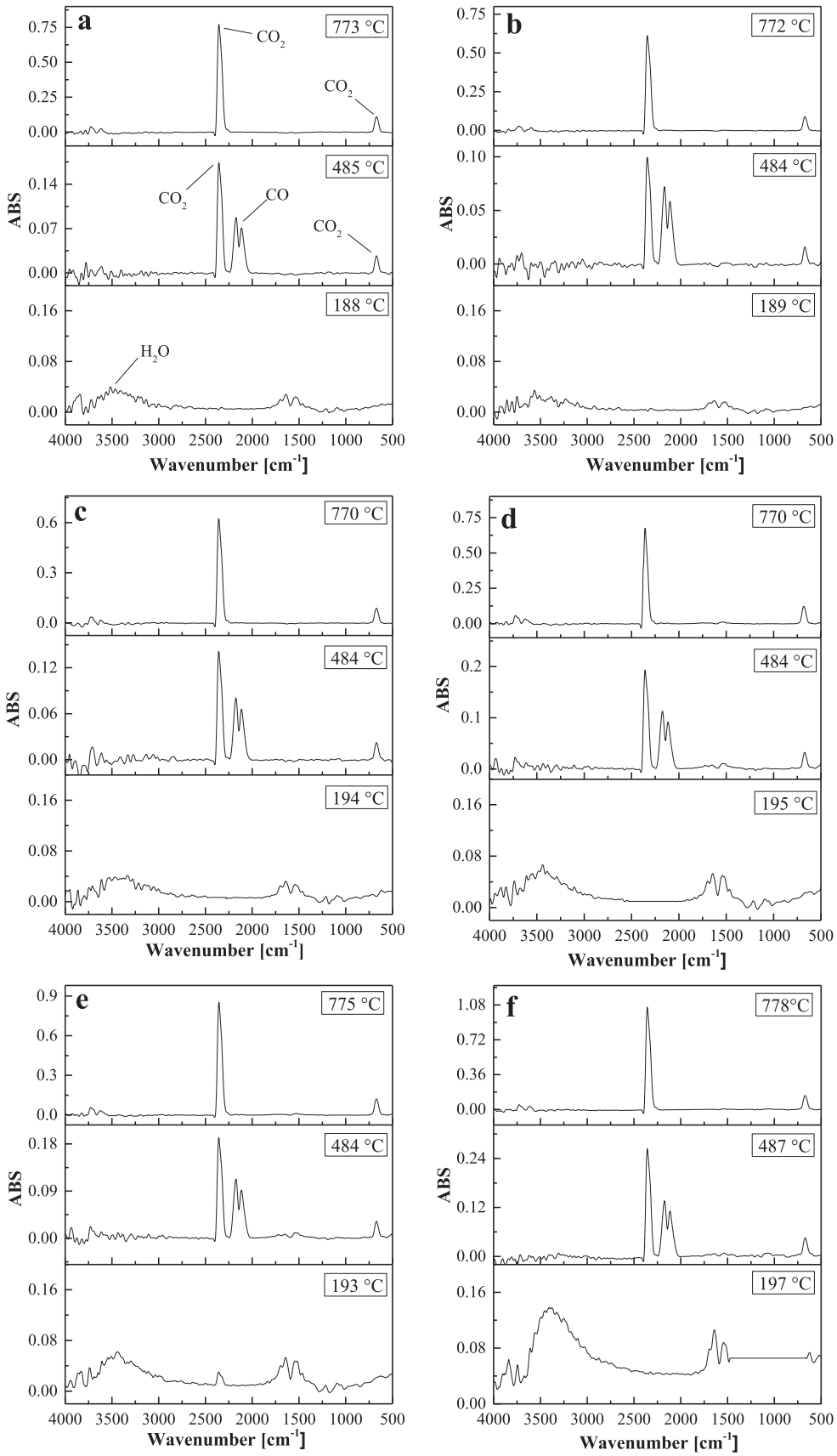

Fig. 9. The instantaneous Fourier-transform infrared spectroscopy (FTIR) spectra of the evolved species during thermal decomposition of the calcium oxalate (CaOx). a) 0 ppm, b) 25 ppm, c) 50 ppm, d) 75 ppm, e) 100 ppm, f) 125 ppm.

higher concentrations of Ala–Gly, only COD form were produced, indicating that COM crystal formation is inhibited. The SEM images showed that Ala–Gly concentration could be a key factor in the process of changing crystal size and morphology. At 125 ppm Ala–Gly, CaOx crystals exhibited a considerably reduced mean particle size of ~1 μm and quadrilateral forms with rounded edges. The results of the ζ potential measurement suggested that Ala–Gly increased the negativity of the surface charge of the CaOx crystals from -5.8 ± 0.6 mV to -27.1 ± 2.9 mV when Ala-Gly concentration is increased from 0 to 125 ppm. As with the other characterizations of the crystals, the TGA results indicated that the CaOx crystals at 50 and 75 ppm Ala–Gly underwent a partial phase transformation from COM to COD, while a complete phase transformation was observed at 100 and 125 ppm Ala–Gly. The results of TGA/FTIR analyses indicated that CaOx crystals underwent three stage decompositions and that H_2O, CO, and CO_2 were the main evolved gases, respectively. Our in-vitro study highlights the role of dipeptide Ala-Gly in dictating the forms of CaOx as well as its morphology and size. We hope that this physiochemical study can inform potential preventative treatments of urinary stones where preferential nucleation of thermodynamically unstable COD, a CaOx phase that is less likely reported to be retained in kidney.

CRediT authorship contribution statement

Sevgi Polat: Conceptualization, Methodology, Investigation, Validation, Visualization, Writing - original draft, Writing - review & editing. **Huseyin Burak Eral:** Conceptualization, Visualization, Writing - original draft, Writing - review & editing, Supervision.

Declaration of Competing Interest

The authors declare that they have no known competing financial interests or personal relationships that could have appeared to influence the work reported in this paper.

References

[1] S. Zaki, N. Jahan, M. Kalim, G. Islam, In vitro antilithiatic activity of the hydro-alcoholic extract of Cinnamomum zeylanicum Blume bark on calcium oxalate crystallization, J. Integr. Med. 17 (4) (2019) 273–281, https://doi.org/10.1016/j.joim.2019.04.001.

[2] P. Chatterjee, A. Chakraborty, A.K. Mukherjee, Phase composition and morphological characterization of human kidney stones using IR spectroscopy, scanning electron microscopy and X-ray Rietveld analysis, Spectrochim. Acta - Part A Mol. Biomol. Spectrosc. 200 (2018) 33–42, https://doi.org/10.1016/j.saa.2018.04.005.

[3] Y. Liu, S. Chen, J. Liu, Y. Jin, S. Yu, R. An, Telmisartan inhibits oxalate and calcium oxalate crystal-induced epithelial-mesenchymal transformation via PPAR-γ-AKT/STAT3/p38 MAPK-Snail pathway, Life Sci. 241 (2020), 117108, https://doi.org/10.1016/j.lfs.2019.117108.

[4] Ê.R. Dias, T.L.M. Freire-Dias, M.S. Alexandre-Moreira, A. Branco, Flavonoid-rich fraction from Pleroma pereirae (Melastomataceae): effects on calcium oxalate crystallization, antioxidant and antinociceptive activities, Eur. J. Integr. Med. 35 (2020), 101095, https://doi.org/10.1016/j.eujim.2020.101095.

[5] P. Peerapen, V. Thongboonkerd, Differential bound proteins and adhesive capabilities of calcium oxalate monohydrate crystals with various sizes, Int. J. Biol. Macromol. 163 (2020) 2210–2223, https://doi.org/10.1016/j.ijbiomac.2020.09.085.

[6] A. Taller, B. Grohe, K.A. Rogers, H.A. Goldberg, G.K. Hunter, Specific adsorption of osteopontin and synthetic polypeptides to calcium oxalate monohydrate crystals, Biophys. J. 93 (5) (2007) 1768–1777, https://doi.org/10.1529/biophysj.106.101881.

[7] X. Wang, M. Wang, J. Ruan, S. Zhao, J. Xiao, Y. Tian, Identification of urine biomarkers for calcium-oxalate urolithiasis in adults based on UPLC-Q-TOF/MS, J. Chromatogr. B Anal. Technol. Biomed. Life Sci. 1124 (2019) 290–297, https://doi.org/10.1016/j.jchromb.2019.06.022.

[8] L.H. Smith, The many roles of oxalate in nature, Trans. Am. Clin. Climatol. Assoc. 113 (2002) 1–20.

[9] C.J. McMulkin, M. Massi, F. Jones, Tetrazoles: Calcium oxalate crystal growth modifiers, CrystEngComm. 17 (2015) 2675–2681, https://doi.org/10.1039/c4ce01717.

[10] F. Ibis, P. Dhand, S. Suleymanli, A.E.D.M. Van Der Heijden, H.J.M. Kramer, H. B. Eral, A combined experimental and modelling study on solubility of calcium oxalate monohydrate at physiologically relevant pH and temperatures, Crystals. 10 (10) (2020) 924, https://doi.org/10.3390/cryst10100924.

[11] V. Tazzoli, C. Domeneghetti, The crystal structures of whewellite and weddellite: re-examination and comparison, Am. Mineral. 65 (1980) 327–333.

[12] S. Deganello, A.R. Kampf, P.B. Moore, The crystal structure of calcium oxalate trihydrate: $Ca(H_2O)_3(C_2O_4)$, Am. Mineral. 66 (7–8) (1981) 859–886.

[13] P. Vijaya, S. Gopi, Aushiq H. Wani, M.V. Rajasekharan, V.K. Subramanian, Effect of ethylenediaminetetraacetic acid (di sodium salt) and aquasoft 330 on crystal growth and morphology of calcium oxalate, Adv. Powder Technol. 23 (2012) 771–778, https://doi.org/10.1016/j.apt.2011.10.006.

[14] C. Conti, M. Casati, C. Colombo, E. Possenti, M. Realini, G.D. Gatta, M. Merlini, L. Brambilla, G. Zerbi, Synthesis of calcium oxalate trihydrate: new data by vibrational spectroscopy and synchrotron X-ray diffraction, Spectrochim. Acta - Part A Mol. Biomol. Spectrosc. 150 (2015) 721–730, https://doi.org/10.1016/j.saa.2015.06.009.

[15] T. Barker, M. Boon, F. Jones, The role of zinc ions in calcium oxalate monohydrate crystallization, J. Cryst. Growth. 546 (2020), 125777, https://doi.org/10.1016/j.jcrysgro.2020.125777.

[16] J. Zhang, L. Wang, W. Zhang, C.V. Putnis, Role of Hyperoxaluria/Hypercalciuria in controlling the hydrate phase selection of pathological calcium oxalate mineralization, Cryst. Growth Des. (2020), https://doi.org/10.1021/acs.cgd.0c0151.

[17] S. Saha, A. Mishra, A facile preparation of rutin nanoparticles and its effects on controlled growth and morphology of calcium oxalate crystals, J. Cryst. Growth. 540 (2020), 125635, https://doi.org/10.1016/j.jcrysgro.2020.12563.

[18] O.W. Moe, M.S. Pearle, K. Sakhaee, Pharmacotherapy of urolithiasis: Evidence from clinical trials, Kidney Int. 79 (4) (2011) 385–392, https://doi.org/10.1038/ki.2010.38.

[19] K. Ramaswamy, D.W. Killilea, P. Kapahi, A.J. Kahn, T. Chi, M.L. Stoller, The elementome of calcium-based urinary stones and its role in urolithiasis, Nat. Rev. Urol. 12 (2015) 543–557, https://doi.org/10.1038/nrurol.2015.208.

[20] L.S. Huang, X.Y. Sun, Q. Gui, J.M. Ouyang, Effects of plant polysaccharides with different carboxyl group contents on calcium oxalate crystal growth, CrystEngComm. 19 (2017) 4838–4847, https://doi.org/10.1039/c7ce00983f.

[21] O.A. Golovanova, V.V. Korolkov, Effect of amino acids on the crystallization kinetics of calcium oxalate monohydrate, Chem. Sustainable Dev. 21 (2013) 381–388.

[22] O.A. Golovanova, V.V. Korolkov, Thermodynamics and kinetics of calcium oxalate crystallization in the presence of amino acids, Crystallogr. Rep. 62 (2017) 787–796, https://doi.org/10.1134/S1063774517050078.

[23] Y.V. Taranets, O.N. Bezkrovnaya, I.M. Pritula, Effect of amino acids and B-group vitamins on nucleation of calcium oxalate monohydrate crystals, J. Cryst. Growth. 531 (2020), 125368, https://doi.org/10.1016/j.jcrysgro.2019.12536.

[24] J. He, R. Lin, H. Long, Y. Liang, Y. Chen, Adsorption characteristics of amino acids on to calcium oxalate, J. Colloid Interface Sci. 454 (2015) 144–151, https://doi.org/10.1016/j.jcis.2015.02.014.

[25] A. Primiano, S. Persichilli, P.M. Ferraro, R. Calvani, A. Biancolillo, F. Marini, A. Picca, E. Marzetti, A. Urbani, J. Gervasoni, A specific urinary amino acid profile characterizes people with kidney stones, Dis. Markers. (2020) 8848225, https://doi.org/10.1155/2020/8848225.

[26] O.A. Golovanova, The particle-size distribution method for studying the crystallization of calcium oxalate in the presence of impurities, Crystallogr. Rep. 64 (2019) 146–151, https://doi.org/10.1134/S1063774519010009.

[27] K.D. Wood, B.L. Freeman, M.E. Killian, W.S. Lai, D. Assimos, J. Knight, S. Fargue, Effect of alanine supplementation on oxalate synthesis, Biochim. Biophys. Acta - Mol. Basis Dis. 1867 (2021), 165981, https://doi.org/10.1016/j.bbadis.2020.165981.

[28] K.R. Cho, E.A. Salter, J.J. De Yoreo, A. Wierzbicki, S. Elhadj, Y. Huang, S.R. Qiu, Growth inhibition of calcium oxalate monohydrate crystal by linear aspartic acid enantiomers investigated by in situ atomic force microscopy, CrystEngComm. 15 (2013) 54–64, https://doi.org/10.1039/c2ce25936b.

[29] A. Gul, P. Rez, Models for protein binding to calcium oxalate surfaces, Urol. Res. 35 (2007) 63–71, https://doi.org/10.1007/s00240-007-0087-3.

[30] S. Narula, S. Tandon, S.K. Singh, C. Tandon, Kidney stone matrix proteins ameliorate calcium oxalate monohydrate induced apoptotic injury to renal epithelial cells, Life Sci. 164 (2016) 23–30, https://doi.org/10.1016/j.lfs.2016.08.026.

[31] S. Li, W. Tang, P. Shi, M. Li, J. Sun, J. Gong, A new perspective of gallic acid on calcium oxalate nucleation, Cryst. Growth Des. 20 (5) (2020) 3173–3181, https://doi.org/10.1021/acs.cgd.0c00044.

[32] S. Li, W. Tang, M. Li, L. Wang, Y. Yang, J. Gong, Understanding the role of citric acid on the crystallization pathways of calcium oxalate hydrates, Cryst. Growth Des. 19 (6) (2019) 3139–3147, https://doi.org/10.1021/acs.cgd.8b01305.

[33] J.M. Ouyang, L. Duan, B. Tieke, Effects of carboxylic acids on the crystal growth of calcium oxalate nanoparticles in lecithin-water liposome systems, Langmuir. 19 (2003) 8980–8985, https://doi.org/10.1021/la0208777.

[34] A. Vargas-Fernández, M. Sánchez, F. Díaz-Soler, P. Vásquez-Quitral, M. Yazdani-Pedram, A. Neira-Carrillo, Effect of functionalized multiwalled cnts on the selective formation of calcium oxalate crystals by electrocrystallization, Cryst. Growth Des. 20 (2020) 661–669, https://doi.org/10.1021/acs.cgd.9b01067.

[35] A. Neira-Carrillo, F. Luengo-Ponce, P. Vásquez-Quitral, M. Yazdani-Pedram, M. S. Fernández, H. Cölfen, J.L. Arias, Sulfonated polymethylsiloxane as an additive for selective calcium oxalate crystallization, Eur. J. Inorg. Chem. 2015 (2015) 1167–1177, https://doi.org/10.1002/ejic.201402063.

[36] P. Vásquez-Quitral, J.T. Arana, M.C. Miras, D.F. Acevedo, C.A. Barbero, A. Neira-Carrillo, Effect of diazotated sulphonated polystyrene films on the calcium oxalate crystallization, Crystals. 7 (2017) 1–13, https://doi.org/10.3390/cryst7030070.

[37] J.A. Wesson, E.M. Worcester, J.G. Kleinman, Role of anionic proteins in kidney stone formation: Interaction between model anionic polypeptides and calcium oxalate crystals, J. Urol. 163 (4) (2000) 1343–1348, https://doi.org/10.1016/S0022-5347(05)67775-0.
[38] V. Fischer, K. Landfester, R. Muñoz-Espí, Stabilization of calcium oxalate metastable phases by oligo (L-glutamic acid): Effect of peptide chain length, Cryst. Growth Des. 11 (2011) 1880–1890, https://doi.org/10.1021/cg200058d.
[39] S. Farmanesh, J. Chung, D. Chandra, R.D. Sosa, P. Karande, J.D. Rimer, High-throughput platform for design and screening of peptides as inhibitors of calcium oxalate monohydrate crystallization, J. Cryst. Growth. 373 (2013) 13–19, https://doi.org/10.1016/j.jcrysgro.2012.09.018.
[40] J.C.Y. Lo, D. Lange, Current and potential applications of host-defense peptides and proteins in urology, Biomed. Res. Int. (2015), 189016, https://doi.org/10.1155/2015/189016.
[41] J. Kahlen, C. Peter, D. Donadio, Molecular simulation of oligo-glutamates in a calcium-rich aqueous solution: insights into peptide-induced polymorph selection, CrystEngComm. 17 (2015) 6863, https://doi.org/10.1039/c5ce00676g.
[42] R.W. Friddle, M.L. Weaver, S.R. Qiu, A. Wierzbicki, W.H. Casey, J.J. De Yoreo, Subnanometer atomic force microscopy of peptide-mineral interactions links clustering and competition to acceleration and catastrophe, Proc. Natl. Acad. Sci. U. S. A. 107 (1) (2010) 11–15, https://doi.org/10.1073/pnas.0908205107.
[43] O. Miyake, K. Yoshimura, T. Yoshioka, T. Koide, A. Okuyama, High urinary excretion level of citrate and magnesium in children: potential etiology for the reduced incidence of pediatric urolithiasis, Urol. Res. 26 (3) (1998) 209–213, https://doi.org/10.1007/s002400050048.
[44] W. Dong, Q. Wu, Dual roles of melamine in the formation of calcium oxalate stones, Cryst. Growth Des. 19 (7) (2019) 3998–4007, https://doi.org/10.1021/acs.cgd.9b00389.
[45] H.M. Rietveld, Line profiles of neutron powder-diffraction peaks for structure refinement, Acta Crystallogr. 22 (1967) 151–152, https://doi.org/10.1107/s0365110x67000234.
[46] W. Zhao, N. Sharma, F. Jones, P. Raiteri, J.D. Gale, R. Demichelis, Anhydrous calcium oxalate polymorphism: a combined computational and synchrotron X-ray diffraction study, Cryst. Growth Des. 16 (10) (2016) 5954–5965, https://doi.org/10.1021/acs.cgd.6b01005.
[47] M.T.D. Orlando, L. Kuplich, D.O. de Souza, H. Belich, J.B. Depianti, C.G. P. Orlando, E.F. Medeiros, P.C.M. da Cruz, L.G. Martinez, H.P.S. Corrêa, R. Ortiz, Study of calcium oxalate monohydrate of kidney stones by X-ray diffraction, Powder Diffr. 23 (2) (2008) 59–64, https://doi.org/10.1154/1.2903738.
[48] M.H. Lin, Y.L. Song, P.A. Lo, C.Y. Hsu, A.T.L. Lin, E.Y.H. Huang, H.K. Chiang, Quantitative analysis of calcium oxalate hydrate urinary stones using FTIR and 950/912 cm^{-1} peak ratio, Vib. Spectrosc. 102 (2019) 85–90, https://doi.org/10.1016/j.vibspec.2019.03.006.
[49] A. Šter, S. Šafranko, K. Bilić, B. Marković, D. Kralj, The effect of hydrodynamic and thermodynamic factors and the addition of citric acid on the precipitation of calcium oxalate dihydrate, Urolithiasis. 46 (2018) 243–256, https://doi.org/10.1007/s00240-017-0991-0.
[50] X.Y. Sun, C.Y. Zhang, P. Bhadja, J.M. Ouyang, Preparation, properties, formation mechanisms, and cytotoxicity of calcium oxalate monohydrate with various morphologies, CrystEngComm. 20 (2018) 75–87, https://doi.org/10.1039/c7ce01912b.
[51] J. Chung, M.G. Taylor, I. Granja, J.R. Asplin, G. Mpourmpakis, J.D. Rimer, Factors differentiating the effectiveness of polyprotic acids as inhibitors of calcium oxalate crystallization in kidney stone disease, Cryst. Growth Des. 18 (9) (2018) 5617–5627, https://doi.org/10.1021/acs.cgd.8b00945.
[52] J.A. Wesson, E.M. Worcester, J.H. Wiessner, N.S. Mandel, J.G. Kleinman, Control of calcium oxalate crystal structure and cell adherence by urinary macromolecules, Kidney Int. 53 (4) (1998) 952–957, https://doi.org/10.1111/j.1523-1755.1998.00839.x.
[53] J. Liu, H. Jiang, X.Y. Liu, How does bovine serum albumin prevent the formation of kidney stone? A kinetics study, J. Phys. Chem. B. 110 (18) (2006) 9085–9089, https://doi.org/10.1021/jp057403b.
[54] V. Uskoković, Dynamic light scattering based microelectrophoresis: main prospects and limitations, J. Dispers. Sci. Technol. 33 (12) (2012) 1762–1786, https://doi.org/10.1080/01932691.2011.625523.
[55] H.P. Lee, D. Leong, C.T. Heng, Characterization of kidney stones using thermogravimetric analysis with electron dispersive spectroscopy, Urol. Res. 40 (3) (2012) 197–204, https://doi.org/10.1007/s00240-011-0428-0.
[56] R.L. Frost, M.L. Weier, Thermal treatment of whewellite - A thermal analysis and Raman spectroscopic study, Thermochim. Acta. 409 (1) (2004) 79–85, https://doi.org/10.1016/S0040-6031(03)00332-0.
[57] D. Hourlier, Thermal decomposition of calcium oxalate: beyond appearances, J. Therm. Anal. Calorim. 136 (2019) 2221–2229, https://doi.org/10.1007/s10973-018-7888-1.
[58] R.L. Frost, M.L. Weier, Thermal treatment of weddellite - A Raman and infrared emission spectroscopic study, Thermochim. Acta. 406 (1–2) (2003) 221–232, https://doi.org/10.1016/S0040-6031(03)00259-4.